

Magneto-Optical Detection of the Spin Hall Effect in Pt and W Thin Films

C. Stamm,¹ C. Murer,¹ M. Berritta,² J. Feng,¹ M. Gabureac,¹ P. M. Oppeneer,² and P. Gambardella¹

¹*Department of Materials, ETH Zürich, 8093 Zürich, Switzerland*

²*Department of Physics and Astronomy, Uppsala University, P.O. Box 516, SE-75120 Uppsala, Sweden*

The conversion of charge currents into spin currents in nonmagnetic conductors is a hallmark manifestation of spin-orbit coupling that has important implications for spintronic devices. Here we report the measurement of the interfacial spin accumulation induced by the spin Hall effect in Pt and W thin films using magneto-optical Kerr microscopy. We show that the Kerr rotation has opposite sign in Pt and W and scales linearly with current density. By comparing the experimental results with *ab initio* calculations of the spin Hall and magneto-optical Kerr effects, we quantitatively determine the current-induced spin accumulation at the Pt interface as $3 \cdot 10^{-12} \mu_B \text{Å}^{-1} \text{cm}^2$ per atom. From thickness-dependent measurements, we determine the spin diffusion length in a single Pt film to be 10 ± 2 nm, which is significantly larger compared to that of Pt adjacent to a magnetic layer.

The spin Hall effect (SHE) converts an electric charge current flowing along a wire into a transverse spin current [1–3], leading to the accumulation of spins at the surface of the wire [15]. In metals, the induced spin polarization is usually detected *indirectly* through its interaction with an adjacent ferromagnet. Experimental methods to measure the SHE rely on the nonlocal resistance in lateral spin valve devices [5], the spin pumping effect [6], and the spin Hall magnetoresistance [7, 8], as well as on the detection of the SHE-induced spin-orbit torques [9–12], which can even reverse the magnetization in heavy metal-ferromagnet bilayers [13, 14]. In such systems, however, magnetization-dependent scattering, interfacial spin-orbit coupling, and proximity effects deeply influence the spin accumulation [15], complicating the determination of the intrinsic SHE in the nonmagnetic metal. Consequently, estimates of the charge-to-spin conversion ratio, namely the spin Hall angle θ_{SH} , and of the spin diffusion length l_s vary by more than one order of magnitude for the same metal [3]. In order to gain fundamental insight into the mechanisms leading to spin accumulation and optimize the spintronic devices that utilize the SHE, it is therefore essential to study the SHE directly in the nonmagnetic metal layers, without the additional complexity of adding a ferromagnet.

A straightforward method to detect the SHE is to measure the resulting spin accumulation through the magneto-optical Kerr effect (MOKE). This technique has been employed to reveal the SHE in semiconductors, where l_s is of the order of a few μm and the spin accumulation can be laterally resolved by polarization-sensitive MOKE microscopy [16, 17]. The situation is much more difficult in the case of a metallic conductor such as Pt, where l_s is just a few nm. Not only is it unfeasible to detect the lateral spin accumulation with optical wavelengths, also the magnitude of the spin accumulation scales with l_s and is, despite the relatively large θ_{SH} , one to two orders of magnitude smaller compared to semiconductors. Nevertheless, first experiments have been performed to directly study the spin accumulation in heavy

metal films by MOKE. A report by van ’t Erve *et al.* [18] claims a spin accumulation signal on an 8 nm thick film of β -W and on a 20 nm thick film of Pt. The apparent sign change of the observed effect is argued to prove that the polarization rotation, amounting to $3 \cdot 10^{-4}$ rad for β -W, is due to the SHE. A follow-up study by Riego *et al.* [19], however, does not support the above conclusions. In that work, magneto-optic ellipsometry measurements with a Kerr rotation detection limit of 10^{-7} rad show that any observed current-induced effect is related to a change of the reflectivity of the sample caused by Joule heating. More recently, Su *et al.* [20] came to similar conclusions, arguing that MOKE detection would require a current density j larger than 10^8 Acm^{-2} . In fact, all three studies [18–20] used j in the order of 10^5 Acm^{-2} , which leads to an estimated Kerr rotation of the order of 10^{-9} rad [20], five orders of magnitude smaller than the rotation reported initially [18]. Alternative optical approaches to detect the spin accumulation in nonmagnetic metals include Brillouin light scattering [21] and second harmonic generation [22]. Using the latter technique, Pattabi *et al.* [22] reported evidence of current induced spin accumulation in Pt, demonstrating also the feasibility of time-resolved studies. However, the interpretation of the second harmonic signal is not as straightforward as for MOKE, since the knowledge of the non-linear susceptibility of the samples is required to obtain quantitative information.

In this work, we demonstrate the unambiguous detection of the SHE in heavy metals using linear magneto-optical measurements combined with current modulation techniques. We use scanning MOKE microscopy with a sensitivity of 5×10^{-9} rad to detect the spin accumulation at the surfaces of Pt and W wires caused by the SHE. Additionally, we perform *ab initio* linear response calculations of the SHE and magneto-optical Kerr rotation [23] caused by the spin accumulation. Comparison of the experimental data with the *ab initio* MOKE calculations provides quantitative values for the spin accumulation, the spin diffusion length, and the spin Hall angle

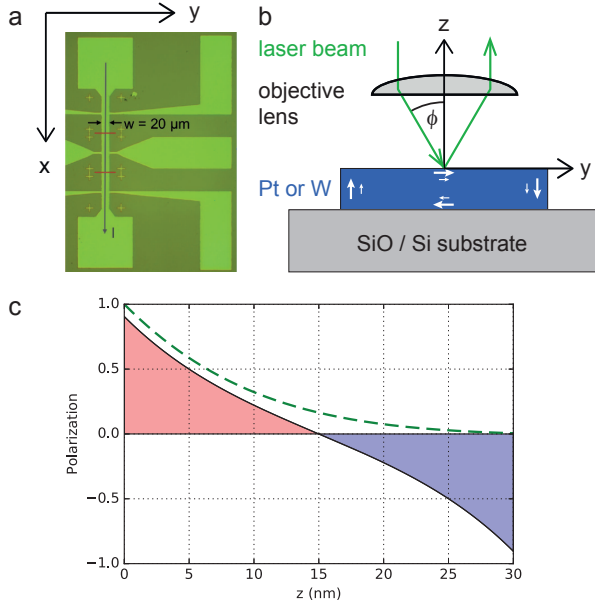


FIG. 1. (a) Microscope image of a Pt Hall bar with the current running top-down (parallel to x). (b) Laser beam path through the focusing objective. The arrows in the Pt or W wire represent the spin accumulation. (c) Depth profile of the calculated spin accumulation (shaded) in a 30 nm thick wire for $l_s = 9$ nm. The dashed line represents the depth-dependent sensitivity of MOKE.

of Pt. These measurements provide a reliable estimate of the SHE and spin diffusion parameters in a nonmagnetic metal, without an adjacent ferromagnet.

Our samples are lithographically-patterned Hall bars of Pt and W with line widths of 10 and 20 μm [Fig. 1(a)]. The Pt films, with thicknesses ranging between 5 and 60 nm, and 10 nm thick W films are deposited by sputtering on oxidized Si substrates. Four-terminal measurements show that the resistivity of Pt varies between $\rho = 26$ and $16 \mu\Omega\text{cm}$ with increasing thickness, whereas the resistivity of W is $\rho = 163 \mu\Omega\text{cm}$, indicative of β -phase W. For the MOKE measurement, a laser beam with wavelength $\lambda = 514$ nm is focused to $\approx 1 \mu\text{m}$ spot size onto the sample, which is mounted on a piezo scanner. A sine-modulated current with variable amplitude up to $j = 1.5 \cdot 10^7 \text{ Acm}^{-2}$ runs through the central conductor, inducing edge spin accumulation [arrows in Fig. 1(b)]. The resulting light polarization rotation is measured using a sensitive detection scheme comprising a polarization-splitting Wollaston prism and a balanced photodetector. Half of the beam is sent onto a photodiode for measuring changes of the reflected intensity. Both signals are measured by lock-in amplifiers that record the fundamental frequency of the Kerr rotation amplitude and the second harmonic contribution of the reflected intensity. More details about the setup are given in Ref. 24.

In a longitudinal MOKE measurement we detect the

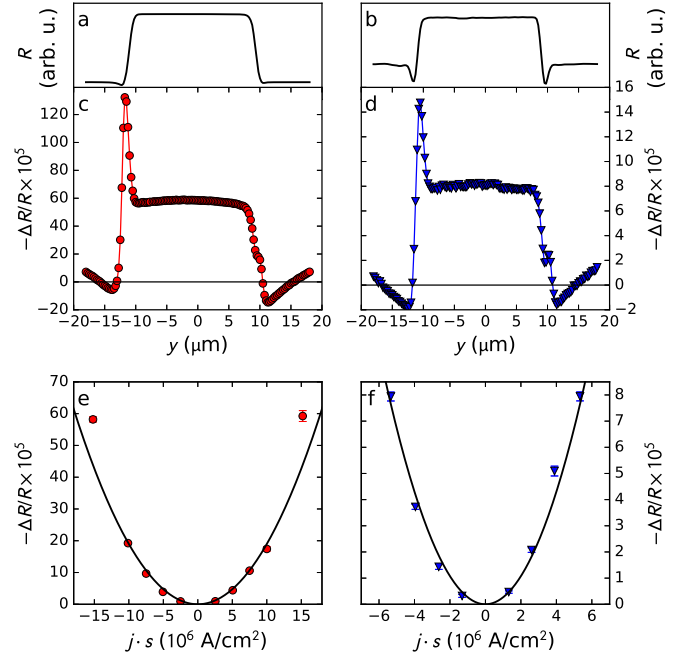


FIG. 2. (a,b) Line scans of the optical reflectivity across 20 μm -wide wires of (a) 15 nm Pt and (b) 10 nm W. (c,d) Thermally induced change of the reflectivity $-\Delta R/R$ for (c) Pt at $j = 1.5 \cdot 10^7 \text{ Acm}^{-2}$ and (d) W at $j = 5.3 \cdot 10^6 \text{ Acm}^{-2}$. (e,f) Current dependence of $-\Delta R/R$ for (e) Pt and (f) W. The solid lines are fits to a j^2 function. Points left of the origin were measured with the reversed optical path, with s denoting the sign of the incidence angle of the laser beam.

accumulation of spins along the in-plane y direction transverse to the electric current flowing along x , as illustrated in Fig. 1(a,b). A consequence of the transverse spin current generated by the SHE is the accumulation of spins of opposite sign at opposite interfaces. We therefore detect the superposition of the polarization rotation from spins accumulated at the top and bottom interfaces, drawn as shaded areas in Fig. 1(c). For quantitative analysis one needs to take into account the light attenuation of the probing laser beam in the conductive material, drawn as dashed line in Fig. 1(c), as modeled by depth-dependent MOKE calculations [19, 26]. At the same time, the material-dependent l_s determines the spatial distribution and the amount of spin accumulation [15], which will be reduced for films of thickness t comparable or smaller than l_s . These effects will lead to a saturation of the spin accumulation detected by MOKE for films of sufficient thickness. From a thickness-dependent study we can therefore extract the intrinsic l_s of a single Pt film, as opposed to the usual Pt/ferromagnetic bilayer.

We first describe the effect of current injection on the optical reflectivity of Pt and W, which is at the origin of controversial MOKE experiments [18–20]. Figure 2 displays the results from scanning the laser beam in the y -direction across the Hall bar while injecting a sinusoidal

current. Both materials, Pt and W, exhibit a change of the reflected intensity R , plotted in Fig. 2. The relative change $\Delta R/R$, measured in the intensity photodiode as second harmonic of the sine current, scales as j^2 and has the same sign in Pt and W. We therefore assign it to temperature-induced changes of the reflectivity [27] due to Joule heating. Using the relationship $\Delta R/R = c_{TR}\Delta T$, where $c_{TR} = -0.58 \cdot 10^{-4} \text{ K}^{-1}$ for Pt [27], we estimate a temperature raise ΔT ranging from 0.16 to 10.1 K as j increases from $2.5 \cdot 10^6$ to $1.5 \cdot 10^7 \text{ Acm}^{-2}$.

Crucial for our study is the Kerr rotation, which is measured as the voltage output of the balanced detector at the fundamental frequency of the driving current and calibrated using a half-wave plate. Figure 3(a,b) show the Kerr rotation angle θ_K measured on 15 nm thick Pt and 10 nm thick W during sinusoidal current injection. We observe a clear Kerr rotation signal from the surface of the conducting wires, which has opposite sign in Pt and W, as expected due to the different sign of the SHE in these two elements, and is of the order of a few tens of nrad. Apart from spurious edge effects, which we attribute to irregular light reflections at the sample boundaries, θ_K is approximately constant over the wire surface, consistent with the spin accumulation picture in Fig. 1(b). Moreover, we find that θ_K varies linearly with the applied current, as shown in Fig. 3(c,d). Linear fits to the data give θ_K/j ratios of $13.9 \pm 0.9 \text{ nrad}/10^7 \text{ Acm}^{-2}$ for Pt and $42.7 \pm 2.1 \text{ nrad}/10^7 \text{ Acm}^{-2}$ for W.

Further evidence that θ_K stems from the accumulated spins at both interfaces and is thus a direct consequence of the SHE in the heavy metal layer comes from the following considerations. First, the sine modulation employed here allows for the harmonic separation of different signal contributions, notably the change of the optical reflectivity proportional to j^2 (Fig. 2) and the linear dependence of θ_K on j (Fig. 3). In contrast, current switching by square wave modulation, as employed in previous studies [18–20], cannot distinguish these effects. We verified that even a slight mismatch between the amplitude of positive and negative current pulses leads to large spurious thermal signals at the fundamental modulation frequency, as discussed also in Ref. 20. Additionally, we implemented an automatic relay scheme that physically inverts the current flowing in the samples and allows us to average out any remaining thermal artifact [24]. Second, control measurements on an Al wire did not result in a detectable Kerr rotation [24], as expected for a light metal with a minute SHE. Third, in the longitudinal Kerr geometry chosen here, we are sensitive to spin signatures in the yz scattering plane, i.e., to the in-plane components along y and perpendicular ones along z . The two contributions exhibit odd and even symmetry upon inversion of the light incidence angle, for the y and z components, respectively. Figure 3(c) and (d) report θ_K measured with opposite angles of incidence in the two halves of each diagram, which prove that the Kerr rotation changes sign

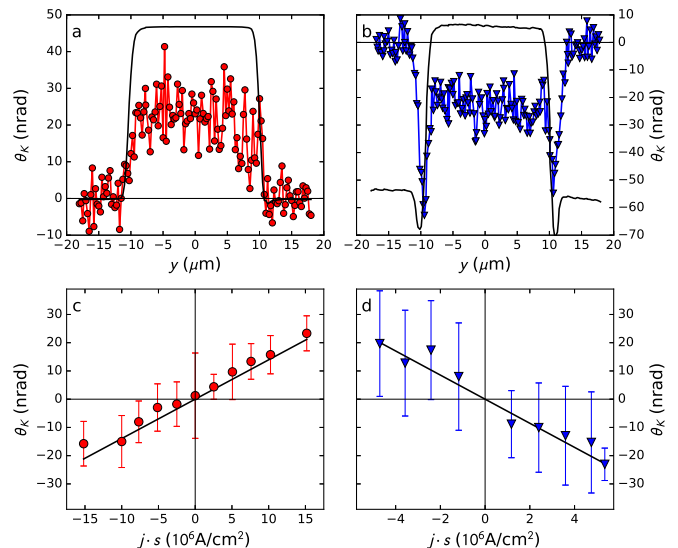


FIG. 3. SHE induced Kerr rotation. (a) Line scan of θ_K across a $20 \mu\text{m}$ wide, 15 nm thick Pt wire at a current density $j = 1.5 \cdot 10^7 \text{ Acm}^{-2}$ and (b) a 10 nm thick W wire at $j = 5.3 \cdot 10^6 \text{ Acm}^{-2}$. (c,d) θ_K as a function of j . The data points represent line scan averages; statistical error bars from averaging multiple line scans are indicated. The solid lines are linear fits to the data. Points left of the origin were measured with the reversed optical path, s denotes the sign of the incidence angle in the MOKE measurement.

by reversing the optical path of the laser beam. The data are fitted by a line that, within error bars, intersects the origin. This also excludes the presence of a polar contribution, i.e., a magnetization along z . As we employed an s-polarized beam, we are not sensitive to the transverse MOKE, which would measure spins oriented along x . We therefore conclude that our signal results from a purely in-plane spin accumulation along y , without detectable perpendicular component.

To relate the measured Kerr rotation to the amount of accumulated spins we performed *ab initio* calculations of the SHE and of the MOKE due to accumulated spins in Pt and W. We use the density-functional theory framework in the local spin-density approximation to compute the relativistic electronic structure, and employ the linear-response theory to calculate the spin- and frequency dependent Hall conductivity $\sigma_{xz}^y(\omega)$ (with y indicating the spin quantization axis) [9] as well as the off-diagonal and diagonal optical conductivities, $\sigma_{ij}(\omega)$ [23]. The DC spin Hall conductivity is given by $\sigma_{xz}^{\text{SH}} = \text{Re}[\sigma_{xz}^{\uparrow}(\omega) - \sigma_{xz}^{\downarrow}(\omega)]/2$, for $\omega \rightarrow 0$. The calculated $\text{Re}[\sigma_{xz}^y(\omega)]$ conductivities of fcc Pt and bcc α -W are shown in Fig. 4(a,b); more details are given in Ref. 24. The spin-dependent Hall conductivities are antisymmetric in the spin projection and the DC spin Hall conductivities of Pt and W have opposite sign. To investigate the possibility of a feedback effect on the SHE due to the spin accumulation, we calculated the spin-

dependent Hall conductivities in the presence of an induced magnetization [dashed curves in Fig. 4(a,b)] and find that its influence is negligible. The calculated spin Hall conductivity of Pt, $\sigma_{xz}^{\text{SH}}(\text{Pt}) = 1890 \Omega^{-1}\text{cm}^{-1}$ is furthermore in agreement with previous calculations ($2000 \Omega^{-1}\text{cm}^{-1}$ [10]) and well within the range of measured values ($\sim 1900 \pm 500 \Omega^{-1}\text{cm}^{-1}$ [14]). Next, we compute the longitudinal Kerr rotation θ_K spectrum for s-polarized light as a function of the induced y -magnetization (M^y) in Pt and W. The results are shown in Fig. 4(c,d), where, for better visibility, we show the curves corresponding to $M^y = 0.01$ and $0.02 \mu_B$ per atom, having verified that θ_K scales linearly with M^y . This information will be used in the following, where we limit the discussion to Pt, for which there is no ambiguity of crystal structure.

We use the *ab initio* calculated σ_{xz}^{SH} and MOKE/ μ_B to compute the spin accumulation in Pt, then compute the theoretical θ_K , and compare it with our experiment. By solving the drift-diffusion equation for spins polarized parallel to y and $-y$ for a film of thickness t [15], we obtain the spin accumulation potential

$$V_s^y(z) = 2l_s \sigma_{xz}^{\text{SH}} \rho^2 j \sinh\left(\frac{t-2z}{2l_s}\right) \left[\cosh\left(\frac{t}{2l_s}\right) \right]^{-1}. \quad (1)$$

The induced magnetization profile can then be calculated as $M^y(z) = \frac{1}{2} e V_s^y(z) \times D(E_F) F \mu_B$, where e is the electron's charge, $D(E_F) = 1.67$ states/eV is the *ab initio* calculated density of states at the Fermi energy, and $F = 2$ is the Stoner enhancement factor of Pt [16]. Using the depth sensitivity of longitudinal MOKE [19] we derive the Kerr rotation expected in a measurement of a thin film [24],

$$\theta_K = \frac{l_s \sigma_{xz}^{\text{SH}} \rho^2 j D(E_F) F e^{\frac{t}{2l_s}}}{2 \cosh(\frac{t}{2l_s})} \times \text{Re} \left\{ \Phi_K^{\text{bulk}} \kappa \left(\frac{(e^{-\kappa^- t} - 1) e^{-\frac{t}{l_s}}}{\kappa^-} - \frac{e^{-\kappa^+ t} - 1}{\kappa^+} \right) \right\}, \quad (2)$$

where Φ_K^{bulk} is the bulk complex Kerr effect, and we have defined $\kappa = (4\pi i \bar{n} \cos \psi) / \lambda$, $\cos \psi = (1 - \sin^2 \phi_i / \bar{n}^2)^{1/2}$, with \bar{n} the complex index of refraction and ϕ_i the angle of incidence, and $\kappa^\pm = \kappa \pm 1/l_s$. From our *ab initio* calculations we obtain values for the spin Hall conductivity, the index of refraction and bulk MOKE [24], while other quantities are given from the experiment (ρ , t , j , ϕ_i).

Figure 5 shows the comparison between the experimental and computed Kerr rotation of Pt as a function of film thickness for a current $j = 10^7 \text{ Acm}^{-2}$. We observe that, after an initial increase, θ_K saturates for $t \gtrsim 30 \text{ nm}$. This behavior can be understood when one considers two effects, the limited probing depth of our optical measurements and the opposite spin accumulation at the top and bottom interfaces due to the SHE. The solid line represents θ_K computed using Eq. (S18) with only l_s as free parameter. We find very good agreement between the

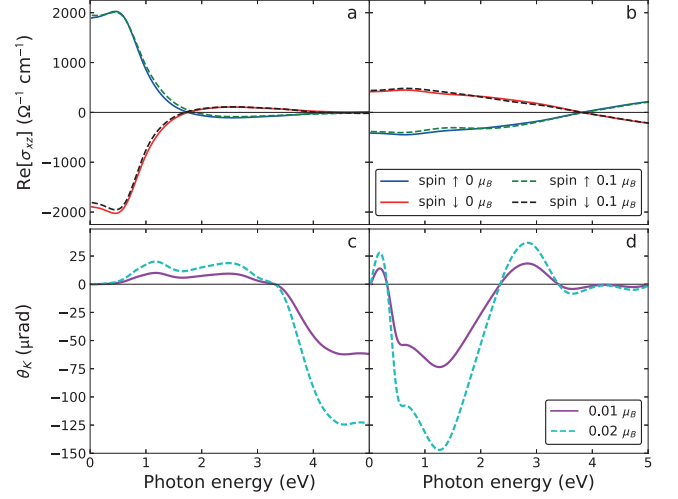


FIG. 4. *Ab initio* spin-resolved Hall conductivity $\text{Re}[\sigma_{xz}^y(\omega)]$ as a function of photon energy $\hbar\omega$ of (a) Pt and (b) W. The influence of a spin accumulation on the calculated $\text{Re}[\sigma_{xz}^y(\omega)]$ is shown by the dashed curves (for an induced magnetization of $M^y = 0.1 \mu_B$ per atom). (c,d) Calculated longitudinal Kerr rotation spectrum for s-polarized light incident at 37° in the yz plane, for $M^y = 0.01 \mu_B$ (magenta line) and $M^y = 0.02 \mu_B$ (dashed cyan line) for Pt and W, respectively.

ab initio and experimental θ_K for $l_s = 8.3 \text{ nm}$. A fit of the data with an unconstrained prefactor in Eq. (S18) (dashed line in Fig. 5) gives $l_s = 10 \pm 2 \text{ nm}$. This is, to our knowledge, the first determination of the intrinsic l_s of a single Pt layer. This l_s , as well as the product $l_s \rho = 1.6 \text{ f}\Omega\text{m}^2$ (for $\rho = 16 \mu\Omega\text{cm}$), are significantly larger than those determined by spin-orbit torque, spin pumping, and magnetoresistance measurements, which typically give $l_s \approx 1 - 2 \text{ nm}$ and $l_s \rho \approx 0.6 - 0.8 \text{ f}\Omega\text{m}^2$ (see [14, 32, 33] for a recent review of experimental results), and in fair agreement with those obtained by nonlocal measurements in lateral spin valve devices, which give $l_s = 11 \pm 2 \text{ nm}$ and $l_s \rho = 1.3 \text{ f}\Omega\text{m}^2$ [34]. The latter measurements, however, are performed at low temperature, where phonon scattering is strongly suppressed compared to our case.

Finally, the spin Hall angle estimated from θ_K for films with $t \geq 40 \text{ nm}$ and $\rho = 15 - 17 \mu\Omega\text{cm}$ is $\theta_{\text{SH}} = 2\sigma_{xz}^{\text{SH}}/\sigma_{xx} = 0.06$, in good agreement with literature data [3]. By computing the proportionality constant between MOKE and the induced magnetization [24], we can also estimate the current-induced magnetization without any assumption on the SHE of Pt. For the 60 nm thick sample, we obtain a magnetic moment at the top interface of $(3.0 \pm 0.4) \cdot 10^{-5} \mu_B/\text{atom}$ and an average moment of $(0.9 \pm 0.1) \cdot 10^{-5} \mu_B/\text{atom}$ in the upper half of the film. Taking into account the MOKE probing depth, we estimate that the total magnetization corresponding to $\theta_K = 40.7 \pm 5.3 \text{ nrad}$ is $(1.4 \pm 0.2) \cdot 10^{-5} \mu_B/\text{atom}$.

In conclusion, we have used MOKE microscopy com-

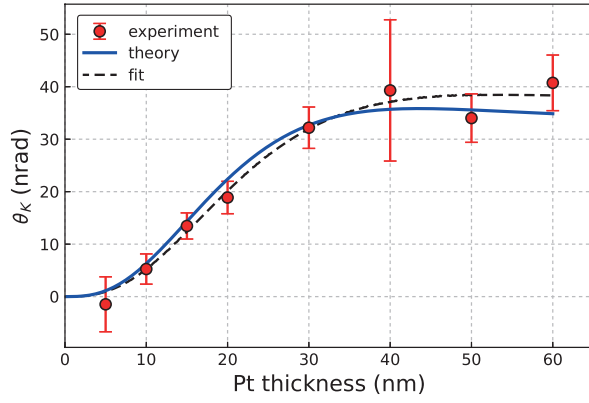


FIG. 5. Kerr rotation in Pt vs. film thickness for $j = 10^7 \text{ Acm}^{-2}$. The symbols are obtained from fitting the experimental Kerr rotation data as shown in Fig. 3. The solid curve is a calculation using Eq. (S18) and $l_s = 8.3 \text{ nm}$. The dashed line is a fit with $\sigma_{xz}^{\text{SH}} \cdot F$ and l_s as free parameters.

combined with *ab initio* calculations of MOKE and spin Hall conductivity to measure the spin accumulation caused by the SHE in Pt and W thin films. Our results demonstrate the feasibility of characterizing the SHE in nonmagnetic metals using magneto-optical methods, independently of the presence of ferromagnets, opening the way to map the spatial and temporal evolution of the spin accumulation and diffusive dynamics in materials with strong spin-orbit coupling and small l_s .

We acknowledge funding by the Swiss National Science Foundation (grant No. 200021-153404), the Swedish Research Council (VR), the K. and A. Wallenberg Foundation (grant No. 2015.0060), and the Swedish National Infrastructure for Computing (SNIC).

[1] M. D'yakonov and V. Perel', JETP Lett **13**, 467 (1971).
[2] J. E. Hirsch, Phys. Rev. Lett. **83**, 1834 (1999).
[3] J. Sinova, S. O. Valenzuela, J. Wunderlich, C. H. Back, and T. Jungwirth, Rev. Mod. Phys. **87**, 1213 (2015).
[15] S. Zhang, Phys. Rev. Lett. **85**, 393 (2000).
[5] S. O. Valenzuela and M. Tinkham, Nature **442**, 176 (2006).
[6] E. Saitoh, M. Ueda, H. Miyajima, and G. Tatara, Appl. Phys. Lett. **88**, 182509 (2006).
[7] H. Nakayama, M. Althammer, Y.-T. Chen, K. Uchida, Y. Kajiwara, D. Kikuchi, T. Ohtani, S. Geprags, M. Opel, S. Takahashi, R. Gross, G. E. W. Bauer, S. T. B. Goennenwein, and E. Saitoh, Phys. Rev. Lett. **110**, 206601 (2013).
[8] C. O. Avci, K. Garello, A. Ghosh, M. Gabureac, S. F. Alvarado, and P. Gambardella, Nat. Phys. **11**, 570 (2015).
[9] K. Ando, S. Takahashi, K. Harii, K. Sasage, J. Ieda, S. Maekawa, and E. Saitoh, Phys. Rev. Lett. **101**, 036601 (2008).
[10] L. Liu, T. Moriyama, D. C. Ralph, and R. A. Buhrman,

Phys. Rev. Lett. **106**, 036601 (2011).
[11] K. Garello, I. M. Miron, C. O. Avci, F. Freimuth, Y. Mokrousov, S. Blugel, S. Auffret, O. Boulle, G. Gaudin, and P. Gambardella, Nat. Nano. **8**, 587 (2013).
[12] X. Fan, H. Celik, J. Wu, C. Ni, K.-J. Lee, V. O. Lorenz, and J. Q. Xiao, Nat. Commun. **5**, (2014).
[13] I. M. Miron, K. Garello, G. Gaudin, P.-J. Zermatten, M. V. Costache, S. Auffret, S. Bandiera, B. Rodmacq, A. Schuhl, and P. Gambardella, Nature **476**, 189 (2011).
[14] L. Liu, C.-F. Pai, Y. Li, H. W. Tseng, D. C. Ralph, and R. A. Buhrman, Science **336**, 555 (2012).
[15] V. Amin and M. Stiles, Phys. Rev. B **94**, 104420 (2016).
[16] Y. K. Kato, R. C. Myers, A. C. Gossard, and D. D. Awschalom, Science **306**, 1910 (2004).
[17] V. Sih, R. C. Myers, Y. K. Kato, W. H. Lau, A. C. Gossard, and D. D. Awschalom, Nat. Phys. **1**, 31 (2005).
[18] O. M. J. van 't Erve, A. T. Hanbicki, K. M. McCreary, C. H. Li, and B. T. Jonker, Appl. Phys. Lett. **104**, 172402 (2014).
[19] P. Riego, S. Velez, J. M. Gomez-Perez, J. A. Arregi, L. E. Hueso, F. Casanova, and A. Berger, Appl. Phys. Lett. **109**, 172402 (2016).
[20] Y. Su, H. Wang, J. Li, C. Tian, R. Wu, X. Jin, and Y. R. Shen, Appl. Phys. Lett. **110**, 042401 (2017).
[21] F. Fohr, S. Kaltenborn, J. Hamrle, H. Schulthei, A. A. Serga, H. C. Schneider, B. Hillebrands, Y. Fukuma, L. Wang, and Y. Otani, Phys. Rev. Lett. **106**, 226601 (2011).
[22] A. Pattabi, Z. Gu, J. Gorchon, Y. Yang, J. Finley, O. J. Lee, H. A. Raziq, S. Salahuddin, and J. Bokor, Appl. Phys. Lett. **107**, 152404 (2015).
[23] P. M. Oppeneer, in *Handbook of Magnetic Materials*, Vol. 13, edited by K. H. J. Buschow (Elsevier, Amsterdam, 2001) Chap. 3, pp. 229 – 422.
[24] See Supplemental Material.
[19] G. Traeger, L. Wenzel, and A. Hubert, Phys. Stat. Sol. (a) **131**, 201 (1992).
[26] J. Hamrle, J. Ferre, M. Nylvlt, and . Visnovsky, Phys. Rev. B **66**, 224423 (2002).
[27] T. Favaloro, J.-H. Bahk, and A. Shakouri, Rev. Sci. Instrum. **86**, 024903 (2015).
[9] P. M. Oppeneer and A. Liebsch, J. Phys.: Condens. Matter **16**, 5519 (2004).
[10] G. Guo, S. Murakami, T.-W. Chen, and N. Nagaosa, Phys. Rev. Lett. **100**, 096401 (2008).
[14] E. Sagasta, Y. Omori, M. Isasa, M. Gradhand, L. E. Hueso, Y. Niimi, Y. Otani, and F. Casanova, Phys. Rev. B **94**, 060412 (2016).
[16] O. Gunnarsson, J. Phys. F: Met. Phys. **6**, 587 (1976).
[32] J.-C. Rojas-Sanchez, N. Reyren, P. Laczkowski, W. Savero, J.-P. Attane, C. Deranlot, M. Jamet, J.-M. George, L. Vila, and H. Jaffrs, Phys. Rev. Lett. **112**, 106602 (2014).
[33] M.-H. Nguyen, D. C. Ralph, and R. A. Buhrman, Phys. Rev. Lett. **116**, 126601 (2016).
[34] Y. Niimi, D. Wei, H. Idzuchi, T. Wakamura, T. Kato, and Y. Otani, Phys. Rev. Lett. **110**, 016805 (2013).

Supplemental Material

EXPERIMENTAL SETUP

Figure S1 shows a detailed schematics of our experimental setup. The sample is mounted on a piezo-controlled xyz -stage for scanning in the xy plane in the laser focus, z being the sample's surface normal. For measuring the longitudinal magneto-optic Kerr effect (MOKE), we use a fiber laser (Origami 10-05 from Onefive GmbH) at $\lambda = 514$ nm wavelength (2.41 eV photon energy), attenuated to a power of $\approx 120 \mu\text{W}$ for Pt and $\approx 20 \mu\text{W}$ for W. The beam is incident in the yz plane, which makes the longitudinal MOKE measurement sensitive to magnetic moments along y . The angle of incidence of $\phi_i \approx 37^\circ$ is achieved by a parallel displacement of the laser beam from the central axis upon entering the objective. As we use s-polarized light, we do not get contributions from the transverse MOKE. The beam is focused on the sample to a spot size of about $1 \mu\text{m}$ by the $100\times$ microscope objective with numerical aperture $\text{NA} = 0.9$.

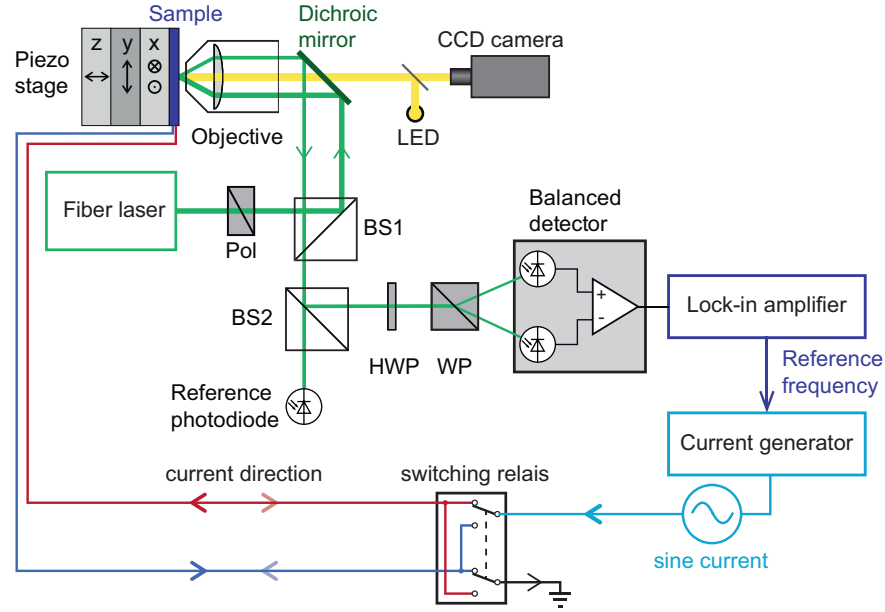


FIG. S1. Schematic drawing of the scanning Kerr effect microscope set-up. The laser beam passes the polarizer (Pol) and first beamsplitter (BS1), is reflected by a dichroic mirror, and enters the objective to be focused onto the sample. The reflected beam is collimated by the same objective, split into two beams at the second beamsplitter (BS2), and its intensity is monitored in the reference photodiode. Light polarization rotation is measured in a second detection branch, comprising of a half wave plate (HWP), Wollaston prism (WP), and balanced photodiode detector.

The intensity and polarization state of the reflected laser beam are measured by a reference photodiode and a balanced detection setup, respectively. The latter comprises a Wollaston prism which splits the light into two beams polarized linearly perpendicular to each other, and a balanced detector to measure their intensity difference. This difference, which is proportional to the polarization rotation, is initially adjusted to zero by rotating a half-wave plate in front of the Wollaston prism. Using a calibration procedure in which we deliberately rotate the polarization axis with the half-wave plate, we determine the proportionality constant between detector output voltage and polarization rotation angle. The signal from the balanced detector is fed into a lock-in amplifier, yielding the spin Hall effect (SHE)-induced Kerr rotation by demodulating at the first harmonic. For measuring changes in the sample's reflectivity, we monitor the reference photodiode's AC component at the second harmonic of the modulation frequency.

The sinusoidally modulated current of frequency 2030 Hz is generated in a voltage-controlled current source driven by the lock-in reference output and passed through the central conductor of the Hall bar patterned on the sample, parallel to the x direction. A relay switch between the current source and the sample reverses the direction of current flow between individual line scans. This procedure allows us to detect the presence of possible asymmetries in the sine-modulated current and, by means of subtracting signals measured with opposite relay switch settings, exclude

Sample	R (Ω)	ρ ($\mu\Omega\text{cm}$)
Pt (5 nm)	478.9	25.7
Pt (10 nm)	198.7	21.7
Pt (15 nm)	149.9	22.7
Pt (20 nm)	108.8	24.5
Pt (30 nm)	62.5	19.5
Pt (40 nm)	36.4	14.8
Pt (50 nm)	33.1	16.3
Pt (60 nm)	29.1	17.4
W (10 nm)	1674.3	162.7
heated W (10 nm)	1216.6	118.2
Al (25 nm)	22.88	5.74

TABLE I. List of measured samples, their resistance R, and resistivity ρ . Four-point probe measurement were done on Hall bar structures over a length of 200 μm .

these effects from the analysis of the Kerr rotation. We found that these asymmetries are negligible when using sine current modulation and lock-in detection, but may become predominant for rectangular pulses of slightly different amplitudes for $+I$ and $-I$.

SAMPLE FABRICATION AND ELECTRICAL CHARACTERIZATION

Pt and W thin films were deposited on oxidized Si(100) wafers by magnetron sputtering. The substrates were cleaned in a 50 $^{\circ}\text{C}$ heated ultrasonic bath first in acetone followed by isopropanol, for 10 minutes each. Sputter deposition with base pressure of $2 \cdot 10^{-8}$ Torr was performed at room temperature. Prior to deposition, further cleaning of the substrate surface was done by argon RF sputtering during 60 s at an Ar partial pressure of 10 mTorr. The Pt samples were deposited in a 0.3 mTorr Ar atmosphere at a growth rate of 1.57 $\text{\AA}/\text{s}$ while rotating the sample holder at 30 rpm. The W films were deposited at a growth rate of 0.041 $\text{\AA}/\text{s}$ in a 5.0 mTorr Ar atmosphere while being rotated at 30 rpm. Finally, the Pt and W thin films were patterned into Hall bar structures (Fig. S2) by photolithography and Ar ion milling.

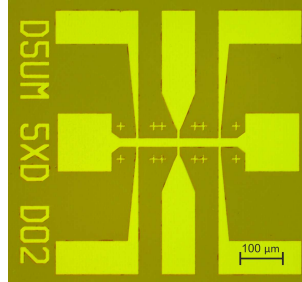


FIG. S2. Image of a photolithographically patterned 10 nm thick Pt sample. Current flows through the horizontal bar, the additional contacts are used to measure the resistance.

Four-point probe resistivity measurements were performed on all samples, as listed in Table I. Literature values for the resistivity of W can reach 260 $\mu\Omega\text{cm}$ for 5.2 nm thick β -W [S1], or 200 $\mu\Omega\text{cm}$ for 12 nm β -W, and 110 $\mu\Omega\text{cm}$ for annealed 12 nm β -W [S2]. For α -W, values between 21 $\mu\Omega\text{cm}$ [S1] and 35 $\mu\Omega\text{cm}$ [S2] are found. We therefore conclude that our sample is predominantly β -W, and that the application of a sine current of 25 mA to a second W sample (denoted as “heated W” in Table I) seems to have heated the sample enough to introduce at least a partial phase change from β -W to α -W.

ABSENCE OF SHE-INDUCED SPIN ACCUMULATION IN ALUMINIUM

In order to test our measurement procedure, we performed additional measurements on a current stripe of Al, a material which is known to have a very small spin Hall angle $\theta_{\text{SH}} \approx 10^{-4}$ [S3]. The results are plotted in Fig. S3, where

no SHE-induced Kerr rotation could be detected within the 5 nrad detection limit, while the reflectivity change is clearly present. Due to the low resistivity of Al, $5.74 \mu\Omega \text{ cm}$, and the resulting lower Joule heating, the thermal-induced change of the optical reflectivity is not as pronounced as for Pt and W.

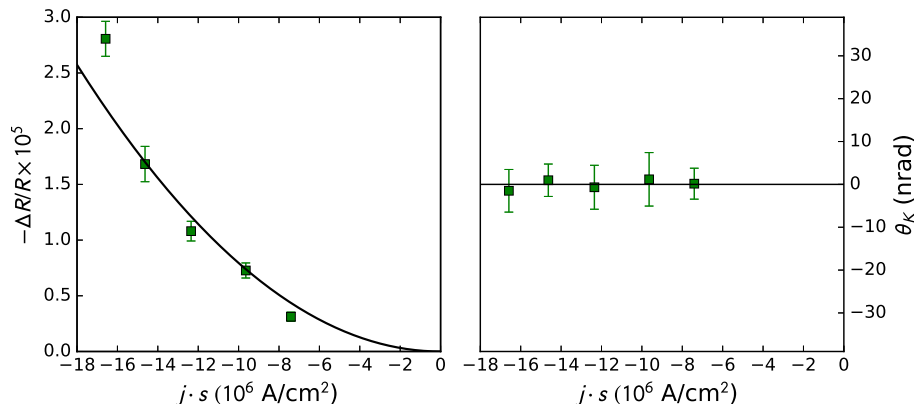


FIG. S3. Comparison measurement on Al showing (a) temperature-induced change of the reflectivity and (b) absence of the SHE-induced Kerr rotation as function of the current density j . The x -scale is multiplied by the sign s of the light incidence angle, for consistency with the data reported in the main text.

THEORETICAL BACKGROUND

We provide here the theoretical background of the detection of the SHE in Pt and W thin metal films using MOKE. Specifically, we employed the linear-response theory combined with the Density Functional Theory (DFT) framework to compute *ab initio* the SHE, the optical response as well as the MOKE response. By comparing the calculated Kerr rotation as a function of film thickness with the experimental data, we obtain values for the spin accumulation, spin Hall angle, and spin diffusion length in Pt. The experiment that we are addressing is schematically depicted in Fig. 1a in the main text. A given current is passed through a thin film of Pt or W and the accumulated magnetization that occurs at the top and bottom surfaces due to the SHE is measured using longitudinal MOKE spectroscopy with the light scattering plane parallel to the yz plane.

To theoretically model the magneto-optical detection of the SHE described in the main text, we have performed the following calculations:

- *Ab initio* calculation of the spin Hall conductivity and conductivity tensor of Pt and W, giving the spin Hall angle.
- Calculation of the spin accumulation at the top and bottom surfaces of the thin films, which is used as input for the *ab initio* calculated spin-resolved conductivity tensor.
- *Ab initio* calculation of the L-MOKE signal for uniformly magnetized materials (Pt and W).
- Calculation of the depth sensitivity of L-MOKE to obtain the theoretical thickness dependent Kerr rotation for a thin film which can be compared with measured values.

We perform the calculations for nonmagnetic fcc Pt and bcc W, with lattice constants $a(\text{Pt}) = 3.9242 \text{ \AA}$ and $a(\text{W}) = 3.1652 \text{ \AA}$, respectively. The theoretical framework and results of the *ab initio* calculations are detailed in the following.

CALCULATIONS OF THE SPIN-RESOLVED CONDUCTIVITY RESPONSE

All our *ab initio* calculations are performed on the basis of the DFT as implemented in the Augmented Spherical Wave (ASW) electronic structure code [S4, S5]. Since we are interested in magnetic features we use the local spin density approximation (LSDA) with the von Barth-Hedin (vBH) parametrization [S6]. This provides us with the relativistic band structure $\epsilon_{n\mathbf{k}}$ of any specific material and with the relativistic eigenstates $|n\mathbf{k}\rangle$ of the Kohn-Sham

Hamiltonian. We then use linear-response theory to calculate most of the relevant quantities that we need to model the experiment which are all related with the conductivity tensor. The optical conductivity tensor is calculated using the linear-response expression [S7, S8]:

$$\sigma_{\alpha\beta}(\omega) = -\frac{i\hbar}{V} \sum_{\mathbf{k}} \sum_{nn'} \frac{f(\epsilon_{n\mathbf{k}}) - f(\epsilon_{n'\mathbf{k}})}{\epsilon_{n\mathbf{k}} - \epsilon_{n'\mathbf{k}}} \frac{\langle n'\mathbf{k} | \hat{j}^\alpha | n\mathbf{k} \rangle \langle n\mathbf{k} | \hat{j}^\beta | n'\mathbf{k} \rangle}{\hbar\omega - \epsilon_{n\mathbf{k}} + \epsilon_{n'\mathbf{k}} + i\hbar/\tau} + \sigma_D(\omega)\delta_{\alpha\beta}. \quad (\text{S1})$$

Here $f(\epsilon_{n\mathbf{k}})$ is the Fermi-Dirac distribution, $\hat{j}^\alpha, \hat{j}^\beta$ are the current density operators in α, β direction and τ is the electron lifetime. The term $\sigma_D(\omega)$ is the Drude contribution to the conductivity,

$$\sigma_D(\omega) = \frac{\sigma_D^0}{1 - i\omega\tau_D}, \quad (\text{S2})$$

where σ_D^0 is the Drude peak amplitude and τ_D is the Drude relaxation time.

The DC spin Hall conductivity can be obtained from computing the spin-resolved, off-diagonal conductivity as given by Eq. (S1) and taking the limit $\omega \rightarrow 0$ (see Ref. [S9]). Adopting here the geometry that the current is along the x direction and the spin quantization axis along y , the corresponding spin-projected off-diagonal conductivity can be written as [S9, S10]:

$$\sigma_{xz}^y = \frac{\hbar}{V} \sum_{\mathbf{k}, n} f(\epsilon_{n\mathbf{k}}) \Omega_n^y(\mathbf{k}), \quad (\text{S3})$$

where we define the Berry curvature (modified by the inclusion of the lifetime) as

$$\Omega_n^y(\mathbf{k}) = \sum_{n' > n} \frac{\text{Im}[\langle n\mathbf{k} | j_x^y | n'\mathbf{k} \rangle \langle n'\mathbf{k} | j_z | n\mathbf{k} \rangle]}{[\epsilon_{n\mathbf{k}} - \epsilon_{n'\mathbf{k}}][\epsilon_{n\mathbf{k}} - \epsilon_{n'\mathbf{k}} + i\hbar/\tau]}. \quad (\text{S4})$$

This equation differs from the equation given in Ref. [S10] due to the inclusion of the lifetime. The quantity $j_x^y = \frac{1}{2}\{s_y, j_x\}$ is the spin current operator for propagation along x and spin axis along y , and $\{\cdot, \cdot\}$ stands for the anti-commutator. Note that we adopt the typical coordinate system of experiments involving thin films, where z is the direction perpendicular to the film plane, rather than that used in the theoretical literature of the SHE, where the off-diagonal conductivity is indicated as $\sigma_{x'y'}^{z'}$, with z' being the spin quantization axis and y' the in-plane direction normal to the current.

The numerical implementation of the matrix elements of the full current operators is described in Ref. [S7] and that of the spin-projected current operators in Ref. [S9]. The k -space integration over the Brillouin zone is performed using the tetrahedron integration method [S7][S11]. We used an electron relaxation time $\hbar\tau^{-1} = 0.02$ Ry (or $\tau = 2.42 \times 10^{-15}$ s) in all our calculations; this value provides a good description of the off-diagonal conductivity of metals [S12].

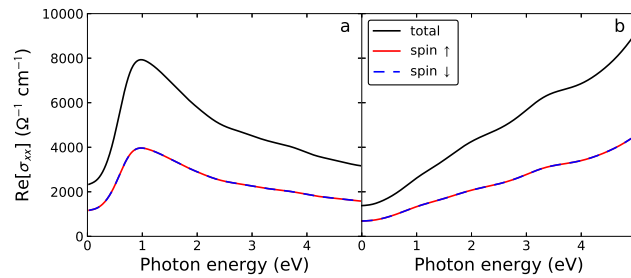


FIG. S4. Spin-resolved diagonal optical conductivity calculated *ab initio* for Pt (a) and W (b) as a function of photon energy $\hbar\omega$.

The *ab initio* calculated results for the real parts of the spin-resolved off-diagonal conductivities of Pt and W (as a function of the photon energy $\hbar\omega$) are shown in Fig. 4 of the main text. The DC spin Hall conductivity is obtained as the limit for $\omega \rightarrow 0$ of the off-diagonal term. Note that the spin-projected off-diagonal conductivity has opposite sign for the spin-up and spin-down contributions, with the total off-diagonal conductivity being zero, as expected for nonmagnetic metals. The spin-resolved diagonal conductivities of Pt and W are shown in Fig. S4. Note that in contrast to the off-diagonal components, the contributions of the spin-up and spin-down channels to the

diagonal conductivity are equal and add up to a total, nonzero conductivity. For Pt we obtain results for the spin Hall conductivity in very good agreement with previous calculations [S10, S13]. Here it is important to note that the authors of Refs. [S10, S13] obtain a factor of two difference between their results. This difference is due to the fact that they used a different definition of the spin Hall conductivity; in Ref. [S10] it is defined as the single spin component conductivity σ_{xz}^\uparrow , or σ_{xz}^\downarrow , while in Ref. [S13] it is represented as $\sigma_{xz}^{\text{SH}} = \sigma_{xz}^\uparrow - \sigma_{xz}^\downarrow$, which, given the fact that we investigate nonmagnetic materials (*i.e.*, with zero off-diagonal total conductivity) is equal to $\sigma_{xz}^{\text{SH}} = 2\sigma_{xz}^\uparrow$. In Table II we compare the results for σ_{xz}^{SH} of Pt as given by the three *ab initio* calculations, and compare to the experimental values [S13, S14], too. Our computed value is somewhat smaller but in good agreement with that obtained by Guo *et al.* [S10]. Moreover, our theoretical value for the SHE conductivity agrees well with the measured value of Zhang *et al.* [S13]. We presume that the theoretical result of Zhang *et al.* [S13] is based on a different definition of the spin Hall conductivity.

Reference	$\sigma_{xz}^{\text{SH}} [\Omega\text{cm}]^{-1}$	Type
This work	1890	theory
Zhang <i>et al.</i> [S13]	4370	theory
Zhang <i>et al.</i> [S13]	1900	experiment
Guo <i>et al.</i> [S10]	2000	theory
Sagasta <i>et al.</i> [S14]	1500-3000	experiment

TABLE II. Comparison of different values of the *ab initio* calculated and measured DC spin Hall conductivity of Pt.

SPIN ACCUMULATION CALCULATIONS

We can now use the values calculated for the spin Hall conductivity to compute the spin accumulation at the top and bottom surfaces of the metal films. For this purpose we solve the drift-diffusion equation in the heavy metal layer, as shown in Ref. [S15] within a Boltzmann transport equation framework. The spin-dependent potential at the surfaces, due to the SHE, is

$$V_s^y(z) = 2l_s\theta_{\text{SH}}\rho j_x \frac{\sinh\left(\frac{t-2z}{2l_s}\right)}{\cosh\left(\frac{t}{2l_s}\right)}, \quad (\text{S5})$$

where l_s is the spin diffusion length in the material, $\theta_{\text{SH}} = 2\sigma_{xz}^{\text{SH}}/\sigma_{xx}$ the spin Hall angle, ρ is the resistivity, t the film thickness, and j_x the current injected in the material. The equation is valid when the diffusion length is reasonably smaller than the thickness, which is fulfilled for most of our samples. Starting from the spin-resolved potential, which can be seen as an effective magnetic field acting on the conduction electrons, we calculate the spin accumulation making use of the equation

$$M^y(z) = \frac{1}{2}V_s^y(z)D(E_F)F, \quad (\text{S6})$$

where $D(E_F)$ is the density of states of the material at the Fermi energy and F is the Stoner enhancement factor. As Stoner enhancement factor for Pt we use the value $F = 2$ [S16]. The density of states were calculated using the ASW method within the DFT framework as $D_{\text{Pt}}(E_F) = 1.67$ states/eV and $D_{\text{W}}(E_F) = 0.34$ states/eV. It is important to mention here that an accurate estimation of the DC longitudinal conductivity is required (which enters in Eq. (S5) in the spin Hall angle and in ρ which is its inverse). Even though it would be possible to estimate the bulk conductivity using *ab initio* methods, we prefer to use the experimental DC conductivity ($\sigma_{xx} = 1/\rho$, see Table I) as input for our calculations. The reason is that there is often a variation of this quantity encountered for different samples (due to preparation conditions, microstructure, sample purity, and thickness), which is better accounted for by taking the conductivity measured in the experiments.

CALCULATION OF THE LONGITUDINAL MOKE

The last quantity that we need to model for the experiment is the prediction of the Kerr rotation for a longitudinal MOKE measurement. For the calculations of the complex L-MOKE Kerr effect, $\Phi_K^L = \theta_K^L + i\varepsilon_K^L$, with θ_K^L the rotation

angle and ε_K^L the Kerr ellipticity, we use the following equations, derived in Refs. [S12, S17],

$$\begin{aligned}\theta_K^L + i\varepsilon_K^L &= \frac{iQ\bar{n}n_0}{\bar{n}^2 - n_0^2} \frac{\cos\phi_i \tan\phi_t}{\cos(\phi_i - \phi_t)} \quad (\text{s-polarization}), \\ \theta_K^L + i\varepsilon_K^L &= \frac{iQ\bar{n}n_0}{\bar{n}^2 - n_0^2} \frac{\cos\phi_i \tan\phi_t}{\cos(\phi_i + \phi_t)} \quad (\text{p-polarization}).\end{aligned}\quad (\text{S7})$$

Here ϕ_i is the angle of incidence angle of the beam and ϕ_t the angle of transmission in the sample, Q is the Voigt parameter, defined as $Q = i\varepsilon_{xy}/\varepsilon_{xx}$, with ε_{ij} elements of the dielectric tensor, and $\bar{n} = (n^+ + n^-)/2$, where n^\pm are the refractive indices for \pm circularly polarized eigenmodes in the material. The dielectric tensor is related to the conductivity tensor as (in cgs or Gaussian units),

$$\epsilon(\omega) = \mathbb{1} + \frac{4\pi i}{\omega} \sigma(\omega). \quad (\text{S8})$$

Using the linear response expression (S1) given above, we can calculate *ab initio* the conductivity tensor, from which we can easily obtain the dielectric tensor. Further, the n^\pm refractive indices are given by [S12]

$$(n^\pm)^2 = \epsilon_{xx} \pm i\epsilon_{xy} \sin\phi_t, \quad (\text{S9})$$

which, making a Taylor expansion for $\epsilon_{xy} \ll \epsilon_{xx}$, gives

$$n^+ - n^- \simeq \bar{n}Q \sin\phi_t. \quad (\text{S10})$$

The angles of incidence and transmittance are related through Snell's law,

$$\bar{n} \sin\phi_t = \sin\phi_i, \quad (\text{S11})$$

where $n_0 = 1$ for the refractive index of vacuum. Substitution of the above expressions in Eq. (S7) gives

$$\theta_K^L + i\varepsilon_K^L = -\frac{\epsilon_{xy} \sin 2\phi_i}{2(1 - \epsilon_{xx})[\cos\phi_i(\epsilon_{xx} - \sin^2\phi_i) + \sin^2\phi_i(\epsilon_{xx} - \sin^2\phi_i)^{1/2}]} \quad (\text{s-polarization}), \quad (\text{S12})$$

$$\theta_K^L + i\varepsilon_K^L = -\frac{\epsilon_{xy} \sin 2\phi_i}{2(1 - \epsilon_{xx})[\cos\phi_i(\epsilon_{xx} - \sin^2\phi_i) - \sin^2\phi_i(\epsilon_{xx} - \sin^2\phi_i)^{1/2}]} \quad (\text{p-polarization}). \quad (\text{S13})$$

Due to the dependence of the Kerr rotation angle on ϵ_{xx} and consequently on σ_{xx} , a good choice of the Drude parameters plays a role for the determination of the theoretical Kerr angle. As mentioned before, we prefer to use values of the Drude peak extracted from the average of the measured DC resistivity ρ , given in Table I, and for the Drude lifetime we use the values from Ref. [S18]. To obtain the bare Drude conductivity σ_D we therefore use

$$\sigma_D = \rho^{-1} - \text{Re}[\sigma_{xx}^{inter}(0)], \quad (\text{S14})$$

where $\sigma_{xx}^{inter}(0)$ is the *ab initio* calculated interband contribution to the DC conductivity, shown in Fig. S4. The calculated values of the Drude conductivity are $\sigma_D(\text{Pt}) = 4.6824 \times 10^{-2} (\mu\Omega\text{cm})^{-1}$ and $\sigma_D(\text{W}) = 4.8 \times 10^{-3} (\mu\Omega\text{cm})^{-1}$ for Pt and W, respectively.

Having predicted the surface magnetization of the sample created by the SHE through Eqs. (S5) and (S6) we can now proceed to calculate the expected Kerr rotation in an identical set-up as in the experiment. The experimental measurement were performed with: 1) a photon energy $\hbar\omega = 2.414$ eV of the probing laser, and 2) an angle of incidence of $\phi_i = 37^\circ$. We calculate the longitudinal Kerr rotation angle for a magnetized sample using Eq. (S12) above. The Kerr angles for nonmagnetic Pt and W in their ground state are of course zero. In order to provide a reference, we introduce a fictitious static magnetic field in the calculations, through which we induce a magnetization of $M_{ind}^{ref} = 0.01 \mu_B$ in both Pt and W, and we calculate the nonzero longitudinal Kerr rotation for this magnetized state. The longitudinal Kerr rotation calculated as a function of the photon energy for a magnetization $M_{ind}^{ref} = 0.01 \mu_B$ is shown for Pt and W in Fig. S5 together with the calculated Kerr angle for a twice as large magnetization (obtained by increasing the fictitious magnetic field). This calculation shows, as one would expect, that the Kerr angle at each photon energy increases linearly with the small reference magnetization.

We can now calculate the proportionality constant between the complex Kerr effect and the induced magnetization as the ratio

$$\alpha = \frac{\Phi_K^L}{M_{ind}^{ref}}. \quad (\text{S15})$$

For Pt we obtain $\alpha = (0.925 - 2.618i) \cdot 10^{-3} \text{ rad}/\mu_B$ at a photon energy $\hbar\omega$ of 2.414 eV.

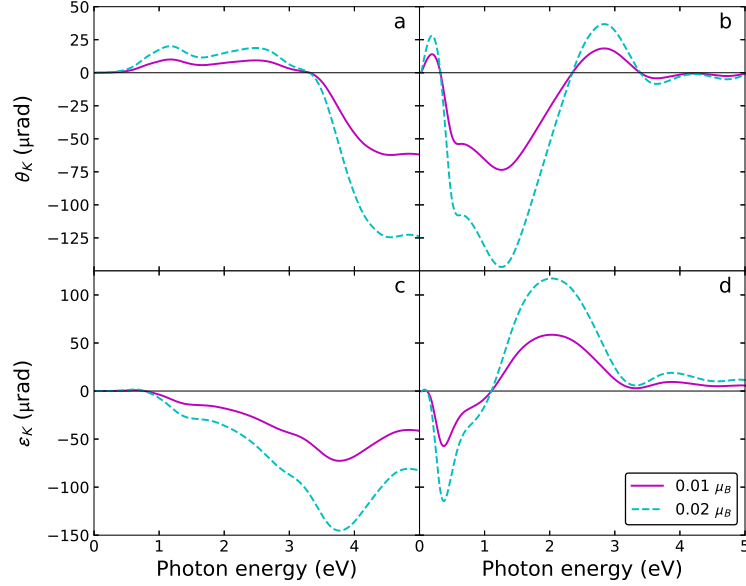


FIG. S5. *Ab initio* calculated Kerr rotation θ_K and ellipticity ε_K for the longitudinal configuration with s-polarized incident light. Results are given for two different induced magnetizations, $M_{ind}^{ref} = 0.01 \mu_B$ (red lines) and $M_{ind}^{ref} = 0.02 \mu_B$ (blue dashed lines), in the left panels for Pt and in the right panels for W. For both metals we show the Kerr effect considering a Drude peak defined by the average resistivity of the thin film samples.

DEPTH SENSITIVITY OF THE LONGITUDINAL MOKE

For a more accurate calculation of the expected Kerr effect in the experiment we need to consider the depth sensitivity of MOKE [S19] and that the spin accumulation is not constant over the thickness of the film. If we consider a material uniformly magnetized, each layer $[z, z + dz]$ of the material will provide a Kerr effect contribution:

$$d\Phi_K^L(z) = \Phi_K^L(z) \frac{4\pi i \bar{n}}{\lambda} e^{-\frac{4\pi i \bar{n} z}{\lambda}} dz, \quad (S16)$$

where λ is the wavelength of the probing laser. Combining this equation with Eqs. (S5) and (S6) we can calculate the expected complex Kerr rotation for a film with thickness t as

$$\Phi_K^{L,tot} = \int_0^t M_s(z) \alpha \frac{4\pi i \bar{n}}{\lambda} e^{-\frac{4\pi i \bar{n} z}{\lambda}} dz. \quad (S17)$$

The complex refractive index $\bar{n} = (n^+ - n^-)/2$ can be easily calculated; we obtain $\bar{n} = 2.12 - 3.79i$ for bulk Pt at 2.414 eV photon energy.

As a next step, we can analytically integrate Eq. (S17) which provides the following expression for the complex longitudinal Kerr effect that is expected in a measurement,

$$\theta_K^m + i\varepsilon_K^m = \frac{l_s \theta_{SH} \rho j_x D(E_F) F \Phi_K^{bulk} e^{\frac{t}{2l_s}}}{2 \cosh(\frac{t}{2l_s})} \kappa \left(\frac{(e^{-\kappa^- t} - 1)e^{-\frac{t}{l_s}}}{\kappa^-} - \frac{e^{-\kappa^+ t} - 1}{\kappa^+} \right), \quad (S18)$$

where we have defined $\kappa = (4\pi i \bar{n} \cos \psi)/\lambda$, $\cos \psi = (1 - \sin^2 \phi_i / \bar{n}^2)^{1/2}$, and $\kappa^\pm = \kappa \pm 1/l_s$. All quantities in Eq. (S18) are obtained from our *ab initio* calculations or defined from experiment (t , j_x) except the spin diffusion length l_s . We can thus use Eq. (S18) to calculate the expected Kerr rotation as a function of film thickness for a given spin diffusion length. We find that the theoretical spin diffusion length that describes best the experimental data is $l_s = 8.3$ nm, which compares well with that obtained from an unconstrained fit of θ_K , as shown in Fig. 5 of the main text.

Lastly, we mention that one can take the real part on both sides of Eq. (S18) and rewrite it to obtain the spin Hall angle θ_{SH} as a function of the other above-mentioned quantities,

$$\theta_{SH} = \frac{\theta_K^m}{j_x} \frac{2 \cosh(\frac{t}{l_s})}{l_s \rho j_x D(E_F) F} \text{Re} \left[\frac{1}{\Phi_K^{bulk}} \frac{\kappa^- \kappa^+}{\kappa [\kappa^+ (e^{-\kappa^- t} - 1) e^{-\frac{t}{l_s}} - \kappa^- (e^{-\kappa^+ t} - 1)]} \right]. \quad (S19)$$

Using this expression one can find the spin Hall angle once the other quantities are known.

-
- [S1] C.-F. Pai, L. Liu, Y. Li, H. W. Tseng, D. C. Ralph, and R. A. Buhrman, *Appl. Phys. Lett.* **101**, 122404 (2012).
 - [S2] Q. Hao, W. Chen, and G. Xiao, *Appl. Phys. Lett.* **106**, 182403 (2015).
 - [S3] S. O. Valenzuela and M. Tinkham, *Nature* **442**, 176 (2006).
 - [S4] A. R. Williams, J. Kübler, and C. D. Gelatt, *Phys. Rev. B* **19**, 6094 (1979).
 - [S5] V. Eyert, *The Augmented Spherical Wave Method* (Springer, Heidelberg, 2007).
 - [S6] U. von Barth and L. Hedin, *J. Phys. C: Solid State Phys.* **5**, 1629 (1972).
 - [S7] P. M. Oppeneer, T. Maurer, J. Sticht, and J. Kübler, *Phys. Rev. B* **45**, 10924 (1992).
 - [S8] R. Mondal, M. Berritta, K. Carva, and P. M. Oppeneer, *Phys. Rev. B* **91**, 174415 (2015).
 - [S9] P. M. Oppeneer and A. Liebsch, *J. Phys.: Condens. Matter* **16**, 5519 (2004).
 - [S10] G. Guo, S. Murakami, T.-W. Chen, and N. Nagaosa, *Phys. Rev. Lett.* **100**, 096401 (2008).
 - [S11] To perform the k -space integration we integrate in the irreducible relativistic wedge of the Brillouin zone over 414720 k -points either for Pt and W.
 - [S12] P. M. Oppeneer, in *Handbook of Magnetic Materials*, Vol. 13, edited by K. H. J. Buschow (Elsevier, Amsterdam, 2001) Chap. 3, pp. 229 – 422.
 - [S13] W. Zhang, M. B. Jungfleisch, W. Jiang, Y. Liu, J. E. Pearson, S. G. te Velthuis, A. Hoffmann, F. Freimuth, and Y. Mokrousov, *Phys. Rev. B* **91**, 115316 (2015).
 - [S14] E. Sagasta, Y. Otori, M. Isasa, M. Gradhand, L. E. Hueso, Y. Niimi, Y. Otani, and F. Casanova, *Phys. Rev. B* **94**, 060412 (2016).
 - [S15] S. Zhang, *Phys. Rev. Lett.* **85**, 393 (2000).
 - [S16] O. Gunnarsson, *J. Phys. F: Met. Phys.* **6**, 587 (1976).
 - [S17] C.-Y. You and S.-C. Shin, *Appl. Phys. Lett.* **69**, 1315 (1996).
 - [S18] M. A. Ordal, R. J. Bell, R. W. Alexander, L. L. Long, and M. R. Query, *Appl. Opt.* **24**, 4493 (1985).
 - [S19] G. Traeger, L. Wenzel, and A. Hubert, *Phys. Stat. Sol. (a)* **131**, 201 (1992).